

VM-Net: Mesh Modeling to Assist Segmentation in Volumetric Data

Udaranga Wickramasinghe, Pascal Fua
Computer Vision Laboratory
EPFL

{udaranga.wickramasinghe, pascal.fua}@epfl.ch

Graham Knott
BioEM Laboratory
EPFL

graham.knott@epfl.ch

Abstract

CNN-based volumetric methods that label individual voxels now dominate the field of biomedical segmentation. In this paper, we show that simultaneously performing the segmentation and recovering a 3D mesh that models the surface can boost performance.

To this end, we propose an end-to-end trainable two-stream encoder/decoder architecture. It comprises a single encoder and two decoders, one that labels voxels and the other outputs the mesh. The key to success is that the two decoders communicate with each other and help each other learn. This goes beyond the well-known fact that training a deep network to perform two different tasks improves its performance.

We will demonstrate substantial performance increases on two very different and challenging datasets.

1. Introduction

State-of-the-Art Volumetric segmentation techniques all rely on Convolutional Neural Networks (CNNs) operating on an image cube. The best architectures usually involve a convolutional encoder that operates on a voxel grid to produce latent features and a convolutional decoder to label the voxels. This was not always so. Deformable surface techniques were once popular [15, 20] because they allowed a user to roughly sketch a shape model and have it deform itself to accurately represent surface details. However, deformable models have now faded because modern segmentation techniques do not require any such initialization and are typically used only for post-processing.

In this paper, we show that these two approaches can work together from the start. To this end, we propose the end-to-end trainable two-stream encoder/decoder architecture. It comprises a single encoder and two decoders depicted by Fig. 1. The first decoder labels voxels, the second outputs a mesh that represents the surface. We will refer to them as the Voxel and Mesh decoders, respectively, and to the whole architecture as **VM-Net**. Not only do the two de-

coders use the same latent features, which tends to add an element of regularization, but even more importantly they communicate with each other. As the resolution increases across successive layers in the voxel decoder, the mesh decoder takes as input the volumetric features produced by the other one at the corresponding scale, as depicted by the gray and blue arrows in the second row of Fig. 1. The intuition behind this design choice is that one should sample first from the lowest resolution features to create a rough surface estimate, then sample from the next higher resolution to refine it, and then repeat until the full resolution is reached.

Our design encourages the voxel features to contribute to good surface reconstruction results. As a result, it also makes them better for segmentation purposes. Thus, we will demonstrate that **VM-Net** outperforms U-Net [3], V-Net [16] and Pixel2Mesh [26] on liver and brain data, even though its architecture and depth are similar, thus evidencing the importance of having one decoder assist the other. Our contribution is therefore to demonstrate that surface modeling still has its place in volumetric data segmentation and we hope to stimulate further research in that direction.

2. Related Work

CNN-based volumetric methods such as U-NET and V-NET [3, 16] now dominate the field of biomedical image segmentation. There have been several recent attempts to further improve these methods, but they have been targeted at specific applications, such as small organ segmentation [18], curvilinear structure segmentation [17, 10]. Some use altogether different design paradigms such as recurrent neural networks that operate on individual slices [29] instead of cubes, but this is generally less effective.

Therefore, even very recent works such as [30, 2] uses U-NET as a backbone or even simpler architectures: The very successful Flood-Filling Networks [7] that were used to segment an impressively large brain volume are encoder-decoder architectures without the long-range skip-connections of U-NET.

Thus, we use U-NET both as the backbone of the segmentation branch of our network and a baseline.

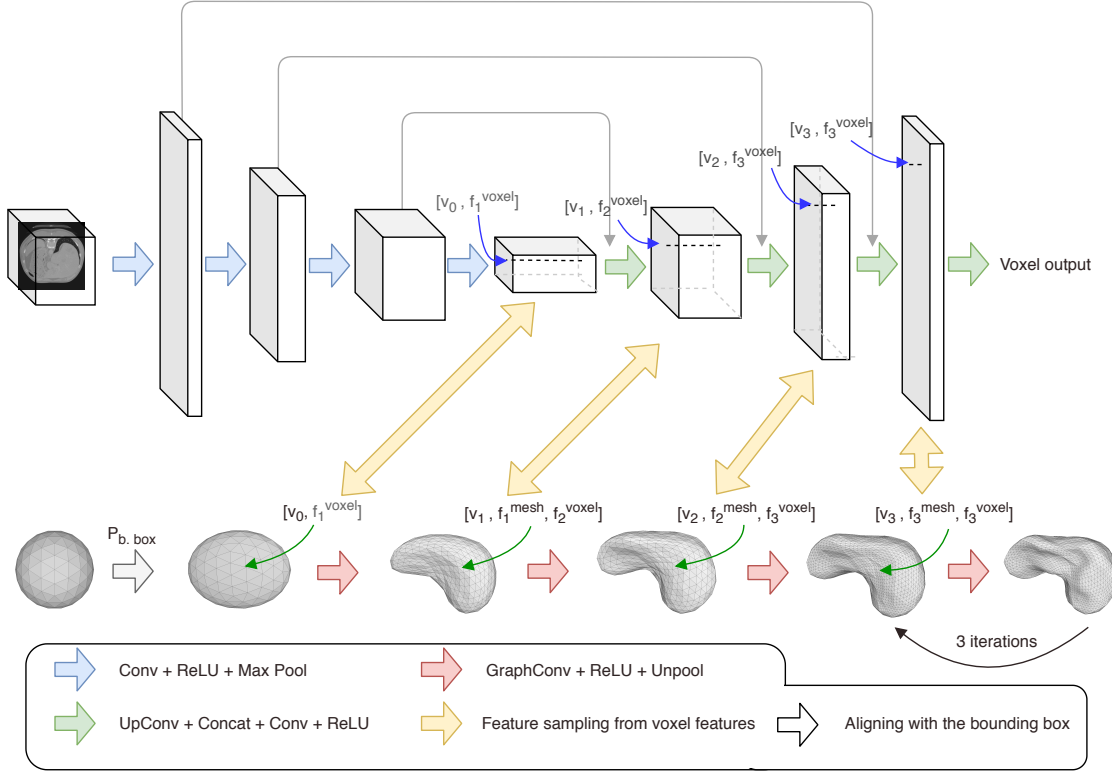


Figure 1. **VM-Net** architecture. The network takes as input an image and sphere mesh. Given the encoder output, the sphere mesh is first aligned with the bounding box $P_{b, box}$ surrounding the object. Afterwards, graph convolution layers iteratively update each vertex. At each stage, for each vertex v_l , we sample voxel features $\mathbf{f}_{l, voxel}^{voxel}$ at v_l (indicated by dark blue arrows). Then sampled feature vector is concatenated with mesh features from previous stage \mathbf{f}_{l-1}^{mesh} and vertex coordinates of v_l to obtain feature vector corresponding to v_l (indicated by dark green arrow). For visualization purpose, the depth dimensions of feature vectors is used to depict feature channel count (best viewed in color).

2.1. Deformable Models

Deformable surface models became popular in the 1990s to model biological structures in volumetric data [6] and new methods keep on being proposed. For example, shape priors were used successfully in [11] to increase the quality of the reconstructions; prior knowledge of shape variability was used in [15, 20] to better fit of deformable membrane templates; in [8] special purpose models were proposed to model thick membranes. However, they all suffer from the fact they require a good initialization that has to be provided by another algorithm, usually a segmentation one. The focus of this paper is to simultaneously perform segmentation and surface recovery, so that no such post processing is required.

There have been some recent attempts at using standard deformable models in conjunction with deep networks [13, 4]. They use CNNs to learn energy functions from the input image instead of directly predicting the surface. Given these energy functions, they perform a traditional energy minimization to deform the surface and there-

fore also require proper initialization.

2.2. Deep Surfaces

A number of deep architectures have recently emerged for the processing of unstructured 3D point clouds [21, 22, 28, 5, 23] and triangulated meshes [14, 25]. But they solely work in a single data representation. That is, they take point clouds or meshes as input and outputs points clouds or meshes.

By contrast, Pixel2Mesh [26] is one of the few recent methods that takes a 2D image as input and outputs a 3D mesh, which is much closer to what we want to do. There are variants of Pixel2Mesh designed to target specific issues in the specialized domain [19, 27] but it remains a prime example of performing these kinds of computation on an image. We therefore adapt so that it can operate on 3D volumes instead of 2D images and used it both as an inspiration for our mesh decoder and as a baseline, as will be discussed in the results section.

3. Method

Fig. 1 depicts our architecture. It takes an image volume as input and returns two outputs, a volume in which the voxels are labeled as foreground or background and a 3D mesh that represents the boundary between the two. This is implemented by a common encoder that produces a latent representation and by two separate decoders, one that generates the segmentation and the other the boundary surface. We will refer to them as the *voxel decoder* and the *mesh decoder* respectively.

Our encoder and volume decoder pictured at the top of Fig. 1 are based on a standard U-Net [3] architecture. By contrast, we had to design a special purpose surface decoder as discussed below.

3.1. Mesh Decoder

As discussed in Section 2, Pix2Mesh proposes an alignment architecture for predicting 3D meshes while transitioning from pixel representation to grid representation. But it was designed for a different purpose. As a result, its encoder starts from the highest-resolution and progressively moves to the lowest. For mesh reconstruction from volumetric images, it makes more sense to sample first from the lowest resolution features to create a rough surface estimate, then sample from the next higher resolution to refine it, and then to repeat until the full resolution is reached. This progression is shown at the bottom of Fig. 1. Note that each stage of the decoder, the voxel features of the appropriate resolution are fed as input along with the surface features, as indicated by the blue arrows.

Architecture The input to the mesh decoder is a sphere with 3D vertices forming facets whose edge we use to perform mesh convolutions. The input sphere is first aligned with the target object on the basis of its bounding box, whose coordinates are predicted by a fully connected network that uses the lowest resolution feature vector as the mesh and voxel decoders. We did not draw it in Fig. 1 for better visual clarity.

Then the aligned mesh is gradually deformed at each stage to match the target object. For each mesh vertex $\mathbf{v}_l = \{x_l, y_l, z_l\}$ whose coordinates are those of the original sphere for $l = 0$ or the output of block l of the decoder, we write

$$\mathbf{f}_{l+1}^{mesh} = h_l(\mathbf{f}_{l+1}^{voxel}, \mathbf{f}_l^{mesh}, \mathbf{v}_l) \quad (1)$$

$$\mathbf{v}_{l+1} = \mathbf{v}_l + \Delta_{l+1}(\mathbf{f}_{l+1}^{mesh}) \quad (2)$$

where \mathbf{v}_{l+1} is the refined vertex at block $l + 1$, \mathbf{f}_l^{voxel} and \mathbf{f}_l^{mesh} are the feature vectors produced by block l and block $l + 1$ in the two mesh and voxel decoder respectively, and h_l and Δ_l are two functions implemented by 4 graph convolution layers each, whose weight we learn during training. By convention, we take \mathbf{f}_0^{voxel} to be an empty feature vector.

We write the graph convolutions as

$$\mathbf{f}_l^i = \frac{1}{|\mathcal{N}(i)| + 1} \sum_{j \in \{i, \mathcal{N}(i)\}} \mathbf{f}_{l-1}^j \mathbf{w}_l, \quad (3)$$

where $\mathcal{N}(i)$ is the neighborhood of \mathbf{v}_i and \mathbf{w}_l a learned set of weights, as in [9]. In our implementation, after the first two mesh convolution blocks, we add an up-sampling layer. We perform uniform edge-split up-sampling, in which each triangular face in the mesh is split in to four triangular faces by splitting each edge in the middle and connecting the new vertices to form four new facets. We not do this for the following layers because the total number of vertices would become too large. In practice, we start with a sphere with 642 vertices end up with 2562 vertices. For each, newly added vertex, we need to define a feature vector associated with it. We compute it by taking the average of the two feature vectors associated with the two vertices of the parent edge.

When sampling features from voxel feature vectors at coordinate \mathbf{v}_l , we use tri-linear interpolation. Instead of only sampling at coordinate \mathbf{v}_l , we sample at additional 26 neighboring points given by coordinates $\mathbf{v}_l = \{x_l \pm \delta, y_l \pm \delta, z_l \pm \delta\}$ where $\delta = \frac{1}{D}$ and D is the length of an edge in input image cube. Since \mathbf{v}_l is in normalized coordinates, we will be sampling the same 26 neighboring points in all resolutions. Afterwards, the sampled 27 points are fed into a single layer perceptron to produce the voxel feature vector associated with vertex \mathbf{v}_l . This neighborhood sampling help extract useful features related to the direction of the vertex update.

As the final stage of the **VM-Net** mesh decoder, we add a iterative refinement operation inspired by similar refinement blocks used in voxel based approaches [12]. Instead of feeding the output mesh back to the first stage of the mesh decoder, we pass it only through the last graph convolution stage. We do this because it samples from the highest resolution feature vectors from the voxel decoder and has been trained to perform the fine refinement. We limit the number of iterations to three as we do not observe any further improvement with additional ones. We only activate the refinement block at inference time.

3.2. Loss functions

We use the cross entropy loss \mathcal{L}_{ce} , the mean square error \mathcal{L}_{mse} , and the Chamfer distance \mathcal{L}_{cf} to train the voxel, alignment, and mesh branches, respectively. The combined loss is therefore taken to be

$$\mathcal{L} = \mathcal{L}_{ce} + \mathcal{L}_{mse} + \sum_{l=1}^L \mathcal{L}_{cf}^l \quad (4)$$

where L is the number of stages in the mesh decoder. We did not find it necessary to add regularization terms to explicitly enforce mesh regularity as this combination already

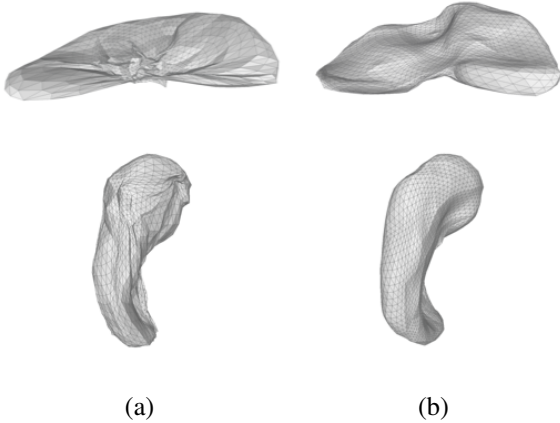


Figure 2. Higher resolution version of the meshes generated by (a) **Vox2Mesh** and (b) **VM-Net**.

yields well behaved meshes with good characteristics and the additional regularization would only degrade the performance.

4. Experiments

In this section, we first introduce the datasets, baselines, and metrics we use to evaluate our approach. We then present our results followed by an ablation study.

4.1. Datasets

We used two very different datasets to test our approach.

Liver Dataset. It consists of 20 labeled CT image cubes from the CHAOS challenge [1]. They are randomly split into 10 training cubes and 10 testing ones. The original images have a 512×512 resolution in x-y plane with varying number of slices in z direction. To keep the computation times practical, we reduced the resolution in the x-y plane to 64×64 and zero padded as necessary in the z direction to create $64 \times 64 \times 64$ image cubes.

Hippocampus dataset It consists of 260 labeled MRI image cubes from the Medical Segmentation Decathlon [24]. We again randomly split it into a training and a testing set of equal sizes. The images have sizes from 32 to 64 in all three dimensions and we zero padded them as needed to produce $64 \times 64 \times 64$ cubes. For training purposes, we used 10 randomly chosen samples from the training set, that is, the same number as in the liver case, except for gauging the influence of the training set size where we used 10, 50, 90 and 130. For testing, we keep a fixed set of 130 samples for all experiments.

4.2. Baselines

As the architecture of our **VM-Net** borrows from both **U-NET** and **Pix2Mesh**, they constitute two natural baselines.

Furthermore, **U-NET** and its **V-NET** variant are widely used in the bio-medical field because these architectures deliver good results while being small enough to handle data cubes, whereas more sophisticated architectures used for 2D image processing cannot easily be adapted for 3D image cubes because their memory requirements are too large. For instance, very recent works like [] use U-Net and/or V-Net as baselines.

As **Pix2Mesh** was not designed to handle data cubes, we use the following variant, which we dub **Vox2Mesh**, in our comparisons. We obtain **Vox2Mesh** by removing mesh projection module in **Pixel2Mesh**. To keep the computational times practical in the volumetric setting, we had to reduce the number of graph convolution layers from 14 to 4. We use the same graph convolution operations and loss function as for **VM-Net**.

4.3. Evaluation Metrics

We use the standard intersection over union (IoU) metric to evaluate our segmentations and the Chamfer distance to evaluate our meshes. The mesh coordinates are normalized and range from -1 to 1 across x,y and z directions. We repeat each experiment three times with different network weight initializations and we report the mean and standard deviation in the tables below.

4.4. Comparative Results

We report our quantitative results on our two datasets in Table 1. **VM-Net** outperforms **U-NET**, **V-NET**, and **Vox2Mesh** on both datasets. In essence, **U-NET** delivers the same results as our voxel decoder would if it were trained alone, without communication with the mesh decoder. Similarly, **Vox2Mesh** delivers the results that our mesh decoder would produce by itself if it had not been trained in conjunction with the voxel decoder and did not use its features as input. The performance boost we observe thus evidences the importance of the collaboration between the two encoders.

As can be seen in Fig. 3 and Fig. 2, the mesh that **VM-Net** produces fits the underlying surface much better than that **Vox2Mesh**. It is much smoother and with almost no self intersections. In-terms of voxel output, although **VM-Net** does not completely eliminate false positives from its segmentation output, their size and number are much reduced and, given the mesh, very easy to identify and remove.

In Table 2, we show the impact of increasing the training set size from 10 to 130 on the hippocampus dataset. **VM-Net** still consistently outperforms **U-NET** but the relative difference tends to decrease. This was to be expected because, the more training data there is, the less necessary the additional regularization constraints that **VM-Net** become. However, in practice, there only rarely is enough training

	Liver		Hippocampus	
	Chamfer Dist. $\times 10^{-3}$	IoU	Chamfer Dist. $\times 10^{-3}$	IoU
V-NET	-	67.4 ± 2.3	-	59.4 ± 2.2
U-NET	-	76.3 ± 3.6	-	70.9 ± 3.5
Vox2Mesh	4.7 ± 0.8	-	2.4 ± 0.3	-
VM-Net	2.3 ± 0.3	79.2 ± 2.0	1.9 ± 0.1	73.5 ± 0.7

Table 1. **Comparative results on our two datasets. VM-Net** outperforms the baselines on both.

Tr. set size	U-NET	VM-Net
10	70.9 ± 3.5	73.5 ± 0.7
50	77.8 ± 0.1	79.3 ± 0.4
90	79.5 ± 0.2	79.9 ± 0.5
130	80.2 ± 0.2	81.3 ± 0.3

Table 2. Increasing the size of the training set.

	Chamfer Dist. $\times 10^{-3}$
Vox2Mesh	4.7 ± 0.8
Vox2Mesh - bottom up	4.3 ± 1.3
+ Voxel decoder	2.8 ± 0.9
+ Voxel decoder + \mathcal{L}_{ce}	2.4 ± 0.4
+ Voxel decoder + $\mathcal{L}_{ce} + \mathcal{L}_{mse}$	2.4 ± 0.3
+ iterative refinement	2.3 ± 0.3

Table 3. Ablation study results summary for the surface decoder on liver datasets

data and additional constraints matter a great deal.

4.5. Ablation Study

To quantify the design choices we made in **VM-Net**, we perform an ablation study on the liver dataset and report our results in Table 4.5. We start from the **Vox2Mesh** baseline. We first modify it by reversing the feature sampling order, that is, instead of first sampling from highest resolution features, we start sampling from the lowest. We dub this version "**Vox2Mesh** bottom-up". Then we add the volume decoder to "**Vox2Mesh** bottom-up" and sample features from the volume decoder instead of the encoder. At this stage, we still don't use \mathcal{L}_{ce} to train the voxel decoder and it is only trained by minimizing \mathcal{L}_{cf} . The next step is to introduce \mathcal{L}_{ce} to train the voxel decoder, and then \mathcal{L}_{mse} to train the module that predicts the bounding box surrounding the object. Finally we add the three iterations of recursive refinement, which results in the full **VM-Net** approach. The results show that the voxel decoder is the larger contributor to the performance boost delivered by **VM-Net**. Next, come the Introduction of \mathcal{L}_{ce} and changing the order of feature sampling in **Vox2Mesh**. The recursive refinement stage also adds a small improvement to the final performance. Using \mathcal{L}_{mse} does not have as clear-cut an impact because its absence can be compensated by the mesh deformation layers. However, the initial alignment module makes large deformations of the mesh unnecessary, making the system

easier to train and more stable as evidenced by the slightly lower variance.

5. Conclusion

We have proposed an end-to-end trainable two stream encoder-decoder architecture that simultaneously produces volumetric and surface descriptions. Crucially, this is more than two decoders working in parallel on a joint latent representation as in many multi-task architectures: The voxel decoder provides features to the mesh decoder at every step, which guarantees that these features are useful for both segmentation and surface reconstruction.

We have demonstrated that this joint architecture performs better than either decoder alone and than the baselines. This confirms the importance of continued surface modeling in biomedical image segmentation. A limitation of the current approach is that it can only handle surfaces of genus 0. In future work, we will explore more sophisticated architectures that can remove this limitation.

References

- [1] Combined (CT-MR) Healthy Abdominal Organ Segmentation (CHAOS). In *International Symposium on Biomedical Imaging*, 2019. 4
- [2] X. Chen and R. Williams. Learning Active Contour Models for Medical Image Segmentation. In *Conference on Computer Vision and Pattern Recognition*, 2019. 1
- [3] Ö. Çiçek, A. Abdulkadir, S. Lienkamp, T. Brox, and O. Ronneberger. 3D U-Net: Learning Dense Volumetric Segmentation from Sparse Annotation. In *Conference on Medical Image Computing and Computer Assisted Intervention*, pages 424–432, 2016. 1, 3
- [4] S. Dong and H. Zhang. A Combined Fully Convolutional Networks and Deformable Model for Automatic Left Ventricle Segmentation Based on 3D Echocardiography. In *BioMed Research International*, 2018. 2
- [5] T. Groueix, M. Fisher, V. Kim, B. Russell, and M. Aubry. Atlasnet: A Papier-Mâché Approach to Learning 3D Surface Generation. In *Conference on Computer Vision and Pattern Recognition*, 2018. 2
- [6] L. He, Z. Peng, B. E., X. Wang, C. Y. Han, K. L. Weiss, and W. G. Wee. A Comparative Study of Deformable Contour Methods on Medical Image Segmentation. *Image and Vision Computing*, 26(2):141–163, 2008. 2

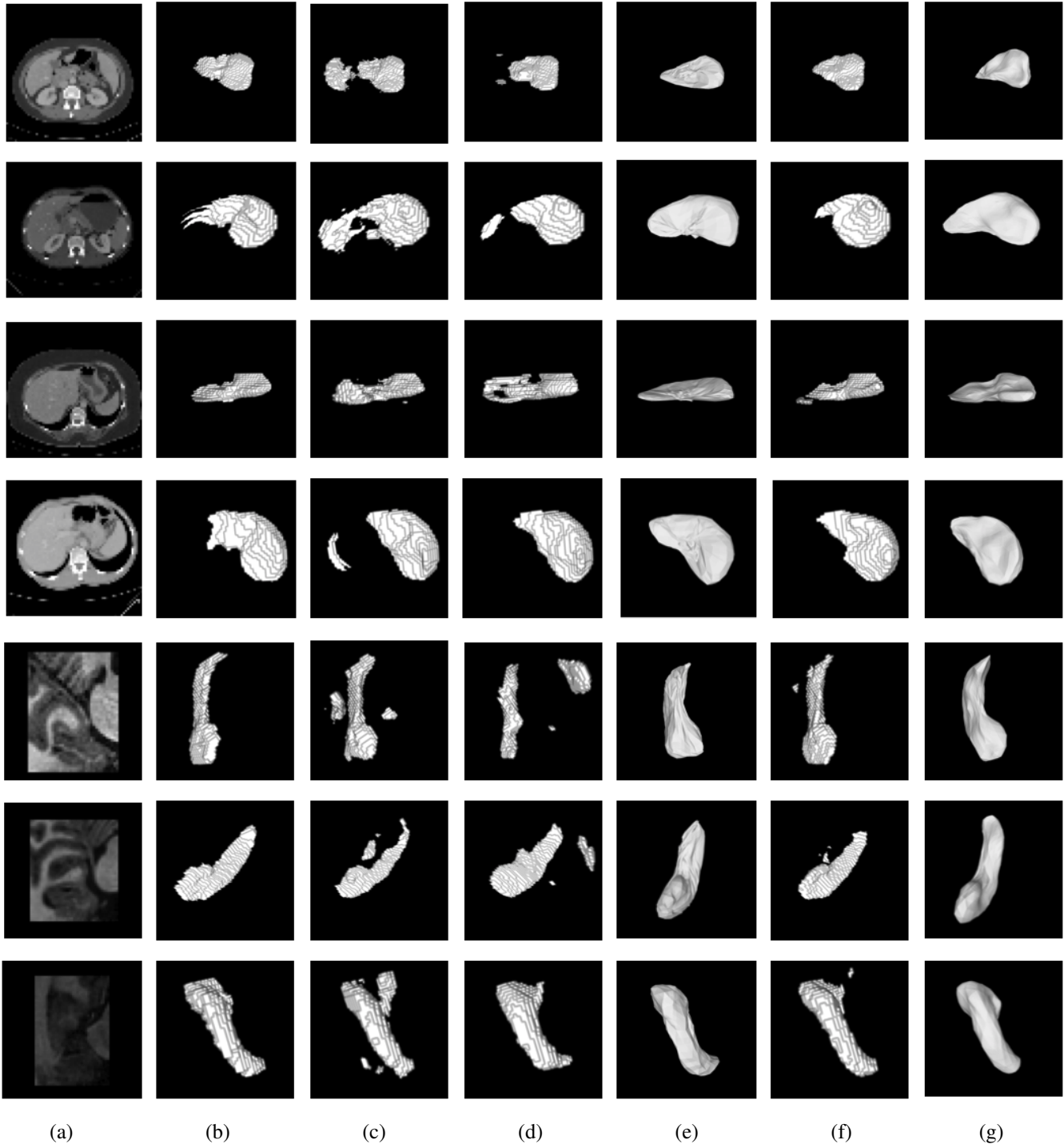


Figure 3. **Comparative results on liver and hippocampus datasets.** Row 1-4 are from the liver dataset and row 4-5 are from hippocampus dataset. (a) Slice from the input volume. (b) Ground truth segmentation. (c) U-NET. (d) V-NET. (e) Vox2Mesh. (f,g) VM-Net voxel and mesh output. We can observe that VM-Net produce improved segmentations compared to U-NET and V-NET. Similarly, we can observe VM-Net produce better meshes compared to VM-Net.

[7] M. Januszewski, J. Kornfeld, P. Li, A. Pope, T. Blakely, L. Lindsey, J. Maitin-Shepard, M. Tyka, W. Denk, and V. Jain. High-Precision Automated Reconstruction of Neurons with

Flood-Filling Networks. *Nature Methods*, 2018. 1
 [8] A. Jorstad, B. Nigro, C. Cali, M. Wawrzyniak, P. Fua, and G.W. Knott. Neuromorph: A Toolset for the Morphometric

- Analysis and Visualization of 3D Models Derived from Electron Microscopy Image Stacks. *Neuroinformatics*, 13(1):83–92, 2014. 2
- [9] T. Kipf and M. Welling. Semi-supervised classification with graph convolutional networks. In *arXiv Preprint*, 2016. 3
- [10] M. Koziński, A. Mosińska, M. Salzmann, and P. Fua. Learning to Segment 3D Linear Structures Using Only 2D Annotations. In *Conference on Medical Image Computing and Computer Assisted Intervention*, pages 283–291, 2018. 1
- [11] M. E. Leventon, W. E. Grimson, and O. Faugeras. Statistical Shape Influence in Geodesic Active Contours. In *Conference on Computer Vision and Pattern Recognition*, pages 316–323, 2000. 2
- [12] X. Liang and J. Feng. Reversible Recursive Instance-level Object Segmentation. In *Conference on Computer Vision and Pattern Recognition*, 2018. 3
- [13] D. Marcos, D. Tuia, B. Kellenberger, and R. Urtasun. Learning deep structured active contours end-to-end. In *Conference on Computer Vision and Pattern Recognition*, 2018. 2
- [14] J. Masci, D. Boscaini, M. M. Bronstein, and P. Vandergheynst. Geodesic Convolutional Neural Networks on Riemannian Manifolds. In *International Conference on Computer Vision*, pages 832–840, December 2015. 2
- [15] T. Mcinerney and D. Terzopoulos. Deformable Models in Medical Image Analysis: A Survey. *Medical Image Analysis*, 1:91–108, 1996. 1, 2
- [16] F. Milletari, N. Navab, and S.-A. Ahmadi. V-Net: Fully Convolutional Neural Networks for Volumetric Medical Image Segmentation. *ArXiv e-prints*, June 2016. 1
- [17] A. Mosińska, K. Tarnawski, and P. Fua. Active Learning and Proofreading for Delineation of Curvilinear Structures. In *Conference on Medical Image Computing and Computer Assisted Intervention*, pages 165–173, September 2017. 1
- [18] A. Novikov, D. Major, M. Wimmer, D. Lenis, and K. Bhlér. Deep sequential segmentation of organs in volumetric medical scans. In *IEEE Transactions on Medical Imaging*, 2019. 1
- [19] J. Pan and K. Jia. Deep Mesh Reconstruction from Single RGB Images via Topology Modification Networks. In *International Conference on Computer Vision*, 2019. 2
- [20] R. Prevos, R. Cuingnet, B. Mory, L.D. Cohen D, and R. Ardon. Incorporating Shape Variability in Image Segmentation via Implicit Template Deformation. *Conference on Medical Image Computing and Computer Assisted Intervention*, pages 82–89, 2013. 1, 2
- [21] C.R. Qi, H. Su, K. Mo, and L.J. Guibas. Pointnet: Deep Learning on Point Sets for 3D Classification and Segmentation. In *Conference on Computer Vision and Pattern Recognition*, 2017. 2
- [22] C.R. Qi, L. Yi, H. Su, and L.J. Guibas. Pointnet++: Deep Hierarchical Feature Learning on Point Sets in a Metric Space. In *Advances in Neural Information Processing Systems*, 2017. 2
- [23] E. Remelli and P. Fua P. Baque. NeuralSampler: Euclidean Point Cloud Auto-Encoder and Sampler. In *arXiv Preprint*, 2019. 2
- [24] A. Simpson and M. Cardoso. A large annotated medical image dataset for the development and evaluation of segmentation algorithms. In *arXiv Preprint*, 2019. 4
- [25] N. Verma, E. Boyer, and J. Verbeek. Feastnet: Feature-Steered Graph Convolutions for 3D Shape Analysis. In *Conference on Computer Vision and Pattern Recognition*, 2018. 2
- [26] N. Wang, Y. Zhang, Z. Li, Y. Fu, W. Liu, and Y. Jiang. Pixel2Mesh: Generating 3D Mesh Models from Single RGB Images. In *European Conference on Computer Vision*, 2018. 1, 2
- [27] C. Wen, Y. Zhang, Z. Li, and Y. Fu. Pixel2Mesh++: Multi-View 3D Mesh Generation via Deformation. In *International Conference on Computer Vision*, 2019. 2
- [28] Y. Yang, C. Feng, Y. Shen, and D. Tian. FoldingNet: Point Cloud Auto-Encoder via Deep Grid Deformation. In *Conference on Computer Vision and Pattern Recognition*, June 2018. 2
- [29] Q. Yu, L. Xie, Y. Wang, Y. Zhou, E. Fishman, and A. Yuille. Recurrent saliency transformation network: Incorporating multi-stage visual cues for small organ segmentation. In *Conference on Computer Vision and Pattern Recognition*, 2018. 1
- [30] A. Zhao and F. Durand. Data augmentation using learned transformations for one-shot medical image segmentation. In *Conference on Computer Vision and Pattern Recognition*, 2019. 1